The Comparison of Biomechanical Breast Models: Initial Results

C. Tanner, J.A. Schnabel, A. Castellano Smith, L.I. Sonoda,

D.L.G. Hill, D.J. Hawkes

Division of Radiological Sciences and Medical Engineering, King's College London, UK

A. Degenhard, C. Hayes, M.O. Leach

Section of Magnetic Resonance, Institute of Cancer Research and

Royal Marsden NHS Trust, Sutton, UK

D.R. Hose,

Department of Medical Physics and Clinical Engineering,

University of Sheffield,

Abstract

We present initial results from evaluating the accuracy with which biomechanical breast models based on finite element methods can predict the displacements of tissue within the breast. We investigate the influence of different tissue elasticity values, Poisson's ratios, boundary conditions, finite element solvers and mesh resolutions on one data set. MR images were acquired before and after compressing a volunteer's breast gently. These images were aligned using a 3D non-rigid registration algorithm. The boundary conditions (surface displacements) were derived from the result of the non-rigid registration or by assuming no patient motion at the posterior or medial side. Three linear and two non-linear elastic material models were tested. The accuracy of the BBMs was assessed by the Euclidean distance of twelve corresponding anatomical landmarks. Overall, none of the tested material models was obviously superior to another regarding the set of investigated values. A major average error increase was noted for partially inaccurate boundary conditions at high Poisson's ratios due to introduced volume change. Maximal errors remained, however, high for low Poisson's ratio due to the landmarks closeness to the inaccurate boundary conditions. Better results were achieved when no boundary conditions were imposed on the posterior side. The choice of finite element solver or mesh resolution had almost no effect on the performance outcome.

Introduction

Biomechanical models constructed using Finite Element Methods (FEM) can be used to model the inter-relation between different types of tissue by applying displacements or forces. This can help to predict mechanical or physical deformation during surgical procedures, and to derive and quantify tissue properties from observed deformations. For example, FEM models for brain modelling have been investigated for model updating of image guided surgery procedures [12], and have been integrated into physically based non-rigid registration methods [8,7]. For imaging of the breast (mammography), FEM models have been explored for predicting mechanical deformations during a biopsy procedure [3], for generating compressions similar to X-ray mammography in MR mammography [16], for improving and testing the reconstruction of elastic properties in elastography [20,14,6], and for the validation of non-rigid registration algorithms [18].

The different biomechanical breast models (BBMs) vary mainly with respect to the mesh generation, boundary conditions used and the assumed tissue properties. The elastic values for the individual tissue types are typically derived from ex-vivo experiments on small specimens. However, only a few studies have been reported [17,9,10,24], and the influence of structures that are connected to the specimens, in-vivo, cannot be measured in this way. The mechanical properties of tissue are likely to change significantly after excision. Further information may come from the field of elastography, where researchers try to solve

the inverse problem by deducing the elastic property distribution from the in-vivo measured displacement field of the tissue for known applied forces to the whole organ. Previous BBMs assume that the nodes adjacent to the pectoral muscle and to any fixed plate have zero displacements [3,16] and that the mobile plates align with the sagittal-plane and moved perpendicular [3].

As the applications for BBMs are very different with respect to both the magnitude of deformation encountered and the required accuracy of prediction, it is important that BBMs are validated for the specific applications for which they were devised. The main sources for inaccurate results from biomechanical FEM models are badly shaped elements, errors with respect to the position of the mesh, the values of the physical properties, the boundary conditions, and the mathematical models or algorithms used for solving. Validation of BBMs is a difficult task itself since the true displacements are unknown. So far, BBMs have been assessed by visual comparison of the simulated compressed breast image with the uncompressed breast [16] or by the displacement errors from three anatomical landmarks selected from the simulation of the compressed breast and the image of an in-vivo compressed breast [3].

In this paper we extended the work in [23] by investigating the accuracy of predicting the breast's deformation only from the displacements on the visible skin surface nodes. The evaluation is based on the acquisition of two breast MR image volumes of one volunteer, with compression plates in two different positions providing two different deformations [22]. A surface displacement field for the breast is calculated by applying a full 3D non-rigid registration [15] to the high resolution 3D pre- and post-deformed images rather than a 3D surface registration [7]. This field is used as a boundary condition for the FEM model. The result of solving the FEM model is then evaluated on the basis of the residual displacement error of manually identified point landmarks. Additionally, the difference images are visually inspected, the tissue displacements are compared with those calculated by the registration algorithm and the average volume change is determined. Experiments were conducted with five BBMs based on the same geometric model, but using linear or non-linear tissue properties for a lateral compression from 74mm to 59mm. These experiments were repeated for a range of different surface boundary conditions. Additionally the influence of the Poisson's ratio, the mesh resolution and the optimisation strategy was assessed.

Physiology of the breast

The female breast is essentially composed of four structures: lobules or glands; milk ducts; fat; connective tissue. The lobules group together into larger units called lobes. On average there are 15 to 20 irregular lobes, which are connected with the nipple via the milk ducts. The breast tissues are joined to the overlaying skin by fibrous strands, called Cooper's ligaments, which emerge from the pectoralis fascia. A stretching or softening of the ligaments, which may occur during pregnancy or with old age, leads to an inferior sagging of the breast in the upright position.

Biomechanical breast models are generally modelling fatty, glandular, cancerous and skin tissue. To our knowledge, the explicit incorporation of Cooper's ligaments into biomechanical breast models has not been attempted to this point. Azar et al. [3] compensated for the effects of Cooper's ligaments by increasing the stiffness of the fatty tissue.

Procedure

MRI data

T1 weighted images of a volunteer were acquired on a Philips 1.5T Gyroscan Intera using a 3D fast gradient echo sequence with TR=16.9, TE=6.0, flip angle 35°, axial slice direction, FOV $210x210x140mm^3$ and a spatial resolution of $0.82x0.82x2mm^3$. A saturation band was used to avoid aliasing of the image of the other breast. The volunteer was positioned in a fixation device for breast biopsies provided by Philips Medical Systems. The right breast was placed between two plates, in the sagittal plane, without any compression for the first image. For the second image, the plate on the breast's medial side was kept immobile, while the plate on the lateral side was moved manually by about 15mm.

The volunteer was asked not to move between these two scans, which were obtained within 10 minutes. Consent of the volunteer was obtained in accordance with the ethical approval LREC number 00/11/99.

Non-Rigid Registration

The non-rigid registration algorithm described in Rueckert et al. [15] was used to register the 3D image of the compressed breast C to the 3D image of the uncompressed breast U. Previously, it was shown that this algorithm significantly improves the image quality of the subtraction images for a cohort of 54 cases [5]. This algorithm employs normalised mutual information as a voxel-similarity measure [21]. It models global motion by a rigid transformation, followed by modelling the breast's deformation by manipulating an underlying mesh of B-spline control points. The combined transformation $T_R : (x, y, z) \mapsto (\widetilde{x}, \widetilde{y}, \widetilde{z})$, which maps any point from the reference image U into its corresponding point in the source image C, is expressed as

$$T_R(x, y, z) = T_{rigid}(x, y, z) + T_{deformation}(x, y, z).$$

The local flexibility and computational complexity of $T_{deformation}$ is related to the FFD resolution defined by the control point spacing. This algorithm makes no assumption about the underlying material properties of the different tissue types in the breast.

The registration algorithm was applied in a multi-resolution fashion, using FFDs with a control point spacing of 20mm followed by 10mm, after an initial rigid registration. The fact that both images were acquired within 10 minutes, in the same setting, with a high resolution and without the administration of contrast agent should facilitate the registration. Additionally, six MR visible markers were placed on the surface of the breast.

Analysis

Geometric FEM Model

The axial 3D MR image of the uncompressed breast (U) was segmented into fatty tissue and glandular tissue using ANALYZE (Biomedical Imaging Resource, Mayo Foundation, Rochester, MN, USA). A 3D triangulation of the outer surface of the fatty tissue was obtained using marching cubes and decimation techniques from vtk [19]. This triangulation was loaded into the ANSYS FEM software package [1] where it was meshed into tetrahedral structural solids (elements) with an additional node in the middle of each edge (SOLID92 [1]). Each node has three associated degrees of freedom which define translations into the nodal x-, y- and z-directions. The elements have quadratic displacement behaviour. Where applicable, the skin was modelled by adding 1mm thick triangles with additional nodes in the middle of each edge (SHELL93 [1]) on the surface of the fatty tissue. Two geometrical models were tested to investigate the combined influence of the element size and shape. ANSYS reports elements to be of 'bad shape' if they either exceeded an aspect ratio of 20 or an angle of 165[o]. Figure 1 shows a 2D example slice of the breast image, the segmentation and the corresponding geometric models before and after solving the FEM.
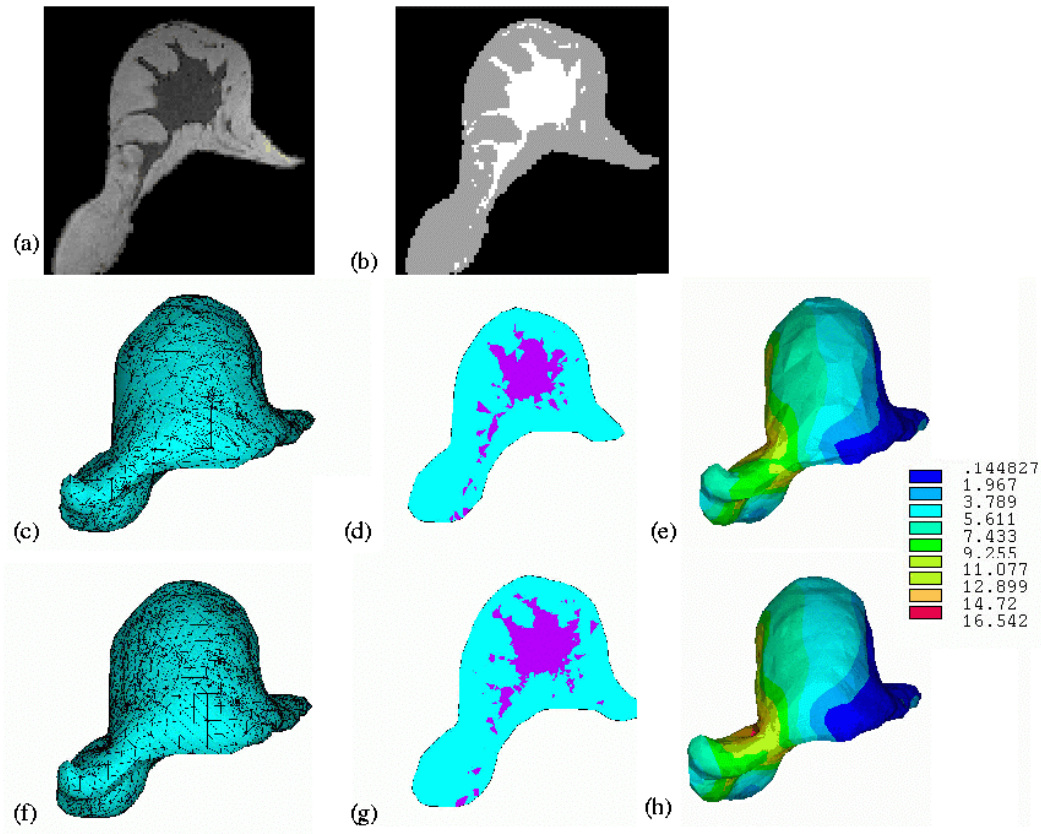
Figure 1 - (a,b) 2D example slice of the 3D MR image showing (a) original 3D MR image of the uncompressed breast, (b) segmentation of (a) into fatty and glandular tissue; (c,d,e) biomechanical breast model GM_1 with (c) surface rendering of undeformed 3D mesh, (d) assignment of fatty and glandular material properties to the elements, (e) deformed 3D mesh with colour encoded displacement magnitude in mm; (f,g,h) same as (c,d,e) for GM_2.

GM_1

This is the coarser geometric model with more badly shaped elements. Firstly, the segmented image was blurred by a Gaussian kernel of one standard deviation and then resampled to 8mm voxel size. Then an initial triangulation of the fat surface was obtained by applying marching cubes. Finally this triangulation was smoothed and decimated by 120 iterations each [19]. This resulted in a final surface with 956 triangles. After meshing, the model had 51072 nodes, 34873 elements and 4484 surface shells. Twenty of these elements were reported by ANSYS as being badly shaped.

GM_2

GM_2 has more elements and less badly shaped elements than GM_1. In comparison with GM_1, only two decimation iterations were applied, resulting in 2662 surface triangles. The final mesh contained 102102 nodes, 4950 surface shells and 72756 elements of which only two were badly shaped.

Material Models

Young's modulus E_n is one of the elastic constants needed to characterise the elastic behaviour of a material. E_n is defined for material n by $E_n = \dfrac{d\sigma_n}{d\varepsilon_n}$ where σ_n and ε_n are the nominal stress and strain, respectively. In a linear material model, E_n does not change for all stress and strain rates.

Published values of the Young's modulus of component tissue of the breast vary by up to an order of magnitude [17,9,10,24], presumably due to the method of measurement or estimation. We constructed models that covered the range of values and complexity of published stress-strain relationships in order to determine their differences in predicting deformations in a systematic and quantitative way.

The breast tissue was modelled as isotropic and homogeneous in all models. The ratio of the strain in lateral direction to that in the axial direction is defined for isotropic material by the Poisson's ratios v. Theoretically, volume is preserved for $v =0.5$. High Poisson's ratio, however, can lead to instabilities (mesh locking) during the approximation process of the finite element method. We therefore investigate the influence of the Poisson's ratio with respect to volume preservation and deformation prediction accuracy. For this, Poisson's ratios of 0.499, 0.495, 0.45, 0.4 and 0.3 were tested. Figure 2 depicts graphically the stress-strain curves for the different models and tissues for strains up to 30%. In the following, the different material models (MMs) are described.
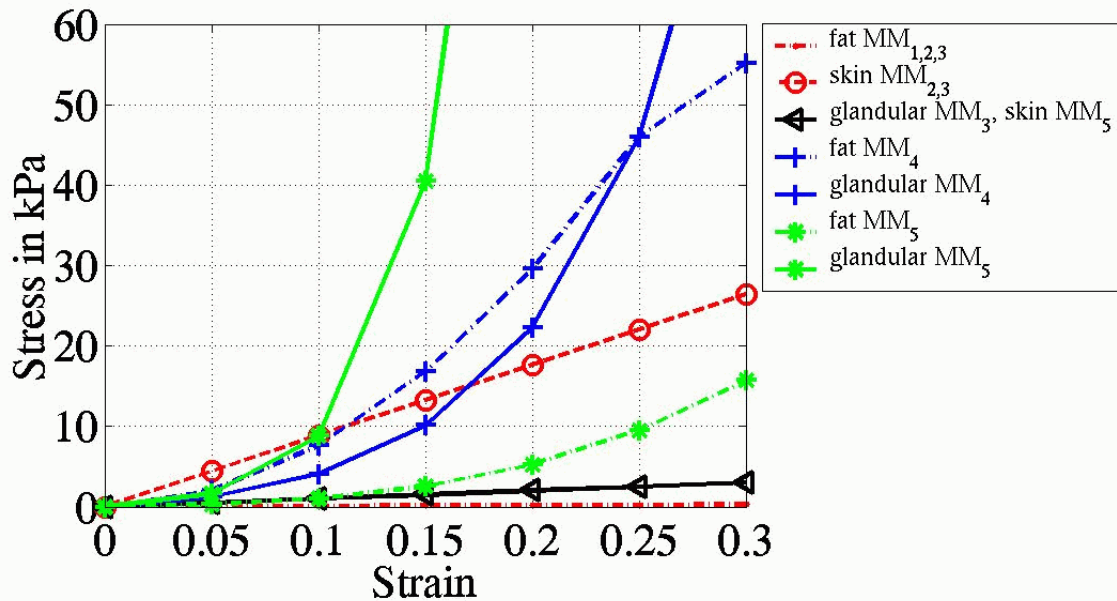
Figure 2 - Piecewise linear approximation of the stress versus strain curves for the breast tissues of the different material models. Straight lines indicate a linear relationship between stress and strain.

MM₁

This is the simplest elastic breast model of the ones compared in this study. The breast tissue was modelled as linear, and a Young's modulus of 1kPa was assigned to fatty and glandular tissue according to published values [17].

MM₂

This model was used in Schnabel et al. [18] to simulate plausible deformations. Fatty and glandular tissues were modelled as in MM₁. Additionally, a Young's modulus of 88kPa was chosen for the skin, representing a linear approximation of the nonlinear stress-strain curve for abdominal skin parallel to the cranio-caudal median investigated by Park [13] for strains up to 30%.

MM₃

This is an extension of MM₂ by incorporating a different Young's modulus of 10kPa for glandular tissue.

MM₄

This non-linear material model was proposed in Azar et al. [3]. It is based on the mechanical properties of breast tissue determined by Wellman [24] with the modification that the Young's modulus of fat increases linearly with strain from zero up to the value for glandular tissue to account for the supporting structure of fibres, including Cooper's ligaments. In Wellman [24], exponential curves were used to describe the stress-strain curves obtained from uniaxial loading of breast tissue:

$$E_n = b \cdot \exp(m\varepsilon_n)$$

where b and m are the fit parameters determined experimentally for every tissue type by Wellman [24]:

$$b_{gland} = 15.1 kPa, \quad m_{gland} = 10.0$$
$$b_{fat} = 4.46 kPa, \quad m_{fat} = 7.4$$

With the modification of Azar et al. [3],

$$E_{fat} = \left[\begin{array}{cc} \left(\dfrac{E_{gland\_avg} - b_{fat}}{\varepsilon_{\lim}} \right)\varepsilon_{fat} + b_{fat} & if \ \varepsilon_{fat} < \varepsilon_{\lim} \\ E_{gland\_avg} & if \ \varepsilon_{fat} \geq \varepsilon_{\lim} \end{array} \right]$$

where E_{gland_avg} is an average stiffness value for glandular tissue and is the calculated Young's modulus of glandular tissue for a limit $\varepsilon_{\lim} = 25\%$ strain: $E_{gland\_avg} = 184 kPa$. In Azar's model the skin is not modeled since it was reasoned that the skin's stiffness is mainly responsible for counteracting the effects of the gravitational force when the patient lies in the prone position and that the applied compression is mainly parallel to the skin's surface.

MM₅

This non-linear model was proposed by Samani et al. [16] and is also based on the mechanical properties of breast tissue determined by Wellman [24]. The stress versus strain curves of this model were created by first fitting quadratic and third-order polynomials to the Young's modulus versus strain data from Wellman [24] of fatty and glandular tissue, respectively, and then integrating over the strain. The fitted Young's modulus (E_n in GPa) versus strain curves were then as follows:

$$E_{fat} = 0.5197 \cdot \varepsilon^2 + 0.0024 \cdot \varepsilon + 0.0049$$
$$E_{gland} = 123.8889 \cdot \varepsilon^3 - 11.7667\varepsilon^2 + 0.6969\varepsilon + 0.0121$$

The skin was modelled as linear tissue with a Young's modulus of 10kPa and a thickness of 1mm. We made an adaptation of this model using a piecewise linear instead of a hyperelastic Neo-Hookean [11] material model.

Boundary Conditions

In order to assess the influence of the boundary conditions (BCs), we have conducted tests with seven different setups. Let Ω_N be the set of all node positions and Ω_S the subset of all surface node positions. Let $T_N : \Omega_N \to \Re^3 : (x, y, z) \mapsto (\breve{x}, \breve{y}, \breve{z})$ be the transformation of the BBM at the node positions.

BC$_1$

In this case, all surface nodes of the FEM model were constrained to the corresponding displacement vectors obtained from the 3D non-rigid registration, i.e. $T_N(x,y,z) = T_R(x,y,z)$ if $(x,y,z) \in \Omega_S$.

BC$_2$

The effects of using only a subset of these surface displacement vectors was assessed in this test. This subset contained all FEM model surface nodes on the posterior, medial and lateral side of the breast. The posterior nodes were defined to be the subset of nodes which were visible when viewing the opaque triangulated breast surface from the posterior side using vtk [19], i.e. the deep surface of the breast. Surface nodes which were within 40mm lateral distance of the most medial node were also selected to belong to the medial side and likewise for the surface nodes within 40mm of the lateral side. In comparison to our previous work [22], we excluded surface nodes posterior of the compression plates from the medial or lateral side to avoid extreme local strains. Boundary conditions derived from the registration were applied to all these nodes, while no boundary conditions were imposed on any of the remaining surface nodes.

BC$_3$

In this test, it was assumed that the pectoral muscle had not moved, i.e. all nodes on the posterior side of the breast were set to have zero displacement ($T_N(x,y,z)=(x,y,z)$). Boundary conditions derived from the registration were applied to the surface nodes on the medial and lateral side as in the test setup of BC$_2$. No boundary conditions were imposed on any other nodes.

BC$_4$

This setup differs from the setup in BC$_3$ only by the assumption that also nodes on the medial side of the breast have not moved, i.e. they have zero displacement.

BC$_5$

This configuration simulate the case of having an optimal surface registration of the breast skin surface without any knowledge of the posterior side. For this, all surface nodes that are visible from the lateral or the medial side at an angle of 40° of the vertical are included in the set of visible nodes. The boundary conditions derived from the non-rigid registration were then only applied to all visible nodes. No boundary conditions were imposed on any other nodes.

BC$_6$

BC$_6$ simulates the case of having a coarser surface correspondance. In this case, about 50% of the visible nodes of BC$_5$ are selected randomly to belong to the set of corresponding surface nodes. Then the boundary conditions derived from the non-rigid registration are applied to the set of corresponding surface nodes. No boundary conditions were imposed on any other nodes.

BC$_7$

BC$_7$ tests a further reduction in corresponding surface nodes. The boundary conditions derived from the non-rigid registration will now only be applied to 5% of the visible nodes of BC$_5$. No boundary conditions were imposed on any other nodes.

FEM Model Solution

All FEM model solutions were obtained using a static or steady state analysis, i.e. the models are assumed to have relaxed to their lowest energy solution. Several methods are available in ANSYS [1] for solving the simultaneous equations generated by the finite element method. The 'Frontal' solver and the 'Sparse Direct' solver are both direct elimination solver. They are recommended when robustness is required. There are several iterative solvers for improving the solution speed. For large models with solid elements, the 'Preconditioned Conjugate Gradient' (PCG) solver is recommended. All models were solved with the PCG solver. The load was applied in one load step. Applying the load in 10 load steps with up to 10 iteration in between gave the same result for linear models. For non-linear model, the maximal difference between the two transformations (max(E_T)) was below 0.01mm. For comparison, we also obtained solutions by the 'Frontal' and the 'Sparse Direct' solver for BC$_2$ and v =0.495.

The ANSYS solution defines a mapping at all node positions which we a call a transformation (T_N). We need a continuous solution for warping an image or evaluating the transformation at any given point. T_N is therefore interpolated by the quadratic shape function for 10-noded tetrahedral elements, in accordance with Davis [4]. Let Ω_M be the set of all positions, which lie within the mesh of the biomechanical model. Let $T_M : \Omega_M \rightarrow \Re^3 : (x, y, z) \mapsto (\breve{x}, \breve{y}, \breve{z})$, be the continuous transformation of T_N.

Landmark Selection

The displacement errors were quantified using twelve corresponding anatomical landmarks. Firstly, two landmarks were selected on each of the slices 10, 20, 30, 40, 50 and 60 of image *C*. Then the corresponding landmarks were selected in image *U*. The landmarks were selected six times by a single observer. The average position from the six measurements was assigned to each landmark. Generally, the landmarks were chosen to lie at the interface between glandular tissue and fatty tissue.

Error Measures

This subsection defines all error measurements employed in this paper.

E_S measures the reproducibility of selecting landmarks. When selecting N_L landmarks N_S times, E_S is given by $E_S = \dfrac{1}{N_L \cdot N_S} \sum\limits_{i=1}^{N_L} \sum\limits_{j=1}^{N_S} \sqrt{(x_K^{ij} - x_K^i)^2 + (y_K^{ij} - y_K^i)^2 + (z_K^{ij} - z_K^i)^2}$ for $K \in \{U, C\}$, where $(x_K^{ij}, x_K^{ij}, x_K^{ij})$ is the position of the *i*th landmark in image *K* at the jth selection and (x_K^i, x_K^i, x_K^i) is the mean position of the ith landmark.

E_L measures the the error of the transformation T_M with respect to the landmarks. For the ith landmark pair this error is given by the Euclidean distance, i.e.

$$E_L^i = \sqrt{(\breve{x}_U^i - x_C^i)^2 + (\breve{y}_U^i - y_C^i)^2 + (\breve{z}_U^i - z_C^i)^2} \ .$$

E_T is used for the comparison of two transformations. Let $T_m : \Omega_m \rightarrow \mathfrak{R}^3 : (x, y, z) \mapsto (\hat{x}, \hat{y}, \hat{z})$ be a transformation produced by either a FEM model or by the 3D non-rigid registration. The difference between T_M and T_m can then be measured at a position $(x,y,z) \in \Omega_{M \cap m}$ by the Euclidean distance

$$E_T = \sqrt{(\breve{x}_U - \hat{x}_U)^2 + (\breve{y}_U - \hat{y}_U)^2 + (\breve{z}_U - \hat{z}_U)^2} \ .$$

E_V and $E_{|V|}$ measure the global and local volume change of the transformation T_M. The volume of a 10-noded tetrahedral element was calculated by integrating the Jacobian of the deformation over the standard simplex. As the deformation is quadratic, the Jacobian matrix is affine. The integration is then equivalent to calculating the determinant of this Jacobian matrix. Since the determinant is rather complex, we calculated the determinant analytically with MAPLE [2] and exported the relevant source code. Let N_E be the number of elements in a model. Let V^i and $\breve{V}^i$ be the volume of the ith element before and after transformation T_M, respectively.

The overall volume change induced by T_M is then given by $E_V = \dfrac{1}{N_E} \dfrac{\sum_{i=1}^{N_E}(\breve{V}^i - V^i)}{\sum_{i=1}^{N_E} V^i}$.

The amount of local volume change can be measured by $E_{|V|} = \dfrac{1}{N_E} \dfrac{\sum_{i=1}^{N_E}|\breve{V}^i - V^i|}{\sum_{i=1}^{N_E} V^i}$.

Analysis Results & Discussion

Figure 3(a) shows 2D orthogonal example slices of the original image pair and the subtraction image. The displacement induced by the plate movement is clearly visible on the subtracted image. The result of the 3D non-rigid registration can be seen in Figure 3(b), where the motion artifacts in the subtracted image have been greatly reduced. Figure 4 illustrates the difference between the boundary conditions BC_2 and BC_3, and the similarity of the material models. The influence of the Poisson's ratio for $BC_{2,3}$ and MM_2 is shown in Figure 5, where an alignment improvement can be noticed with the reduction of v for BC_3. Figure 6 illustrates the spatial distribution of the displacement error E_T between the FEM model prediction and the non-rigid registration displacement field for $BC_{2,3}$ and $v=0.495$. The reduction of this error due to the decrease of Poisson's ratio can clearly be seen for BC_3 in Figure 7. It can be argued that the material models are fairly similar below a strain of 10% and hence the resulting stresses may not differ much. Figure 8 shows the spatial strain distributions for an example slice. Note that only green areas have a strain below 10%.
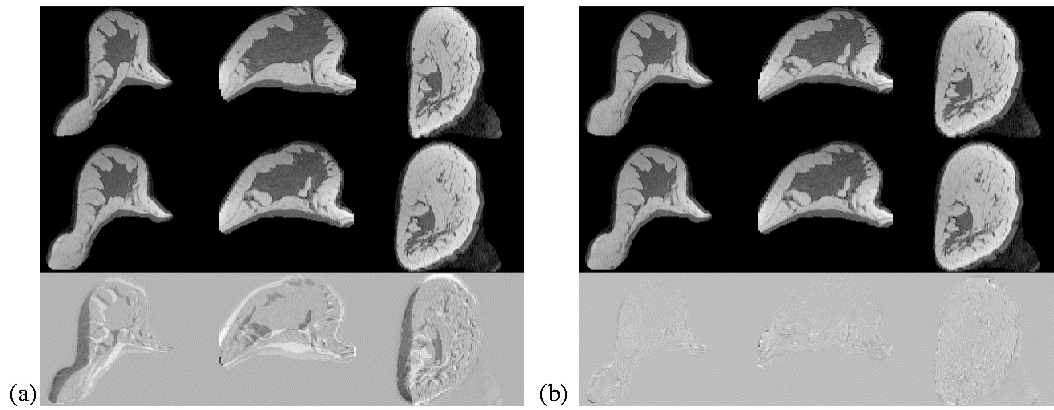
Figure 3 - Axial, sagittal and coronal 2D example slices (a) of the original images. (top) compressed breast; (middle) uncompressed breast; (bottom) subtraction of the middle row from the top row. (b) after applying the 3D non-rigid registration. (top) transformed image of the compressed breast; (middle) uncompressed breast; (bottom) subtraction of the middle row from the top row
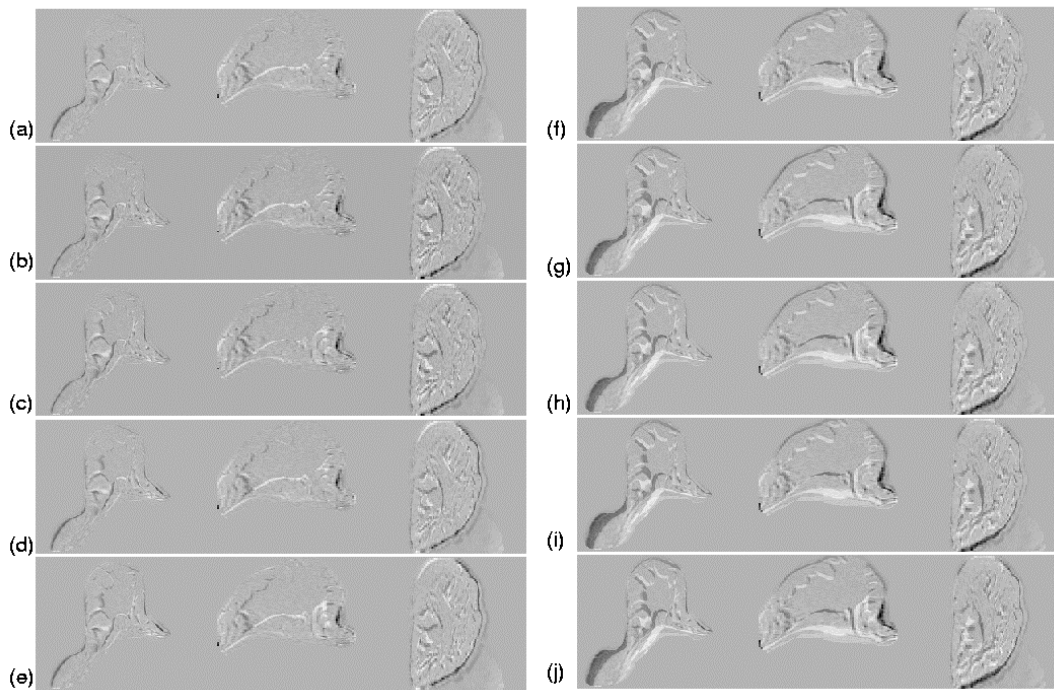
Figure 4 - Orthogonal 2D slices of the subtraction of the deformed image after FEM model simulation from the original image of the compressed breast. (a)-(e) BC_2 MM_{1-5} v =0.495; (f)-(j) BC_3 MM_{1-5} v =0.495.
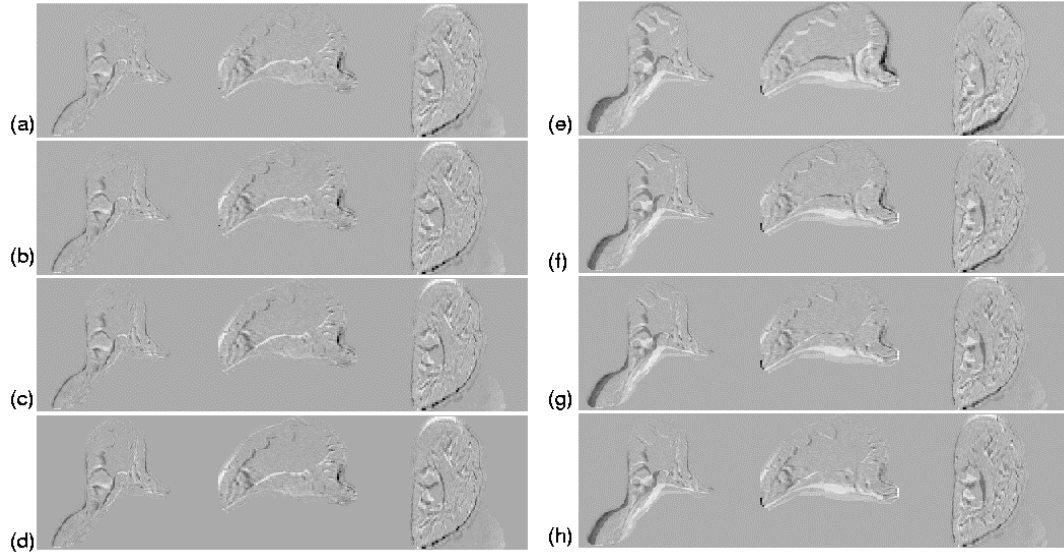
Figure 5 - Orthogonal 2D slices of the subtraction of the deformed image after FEM model simulation from the original image of the compressed breast. (a)-(d) BC_2 MM_2 v =0.499, 0.45, 0.4 and 0.3; (e)-(h) BC_3 MM_2 v =0.499, 0.45, 0.4 and 0.3.
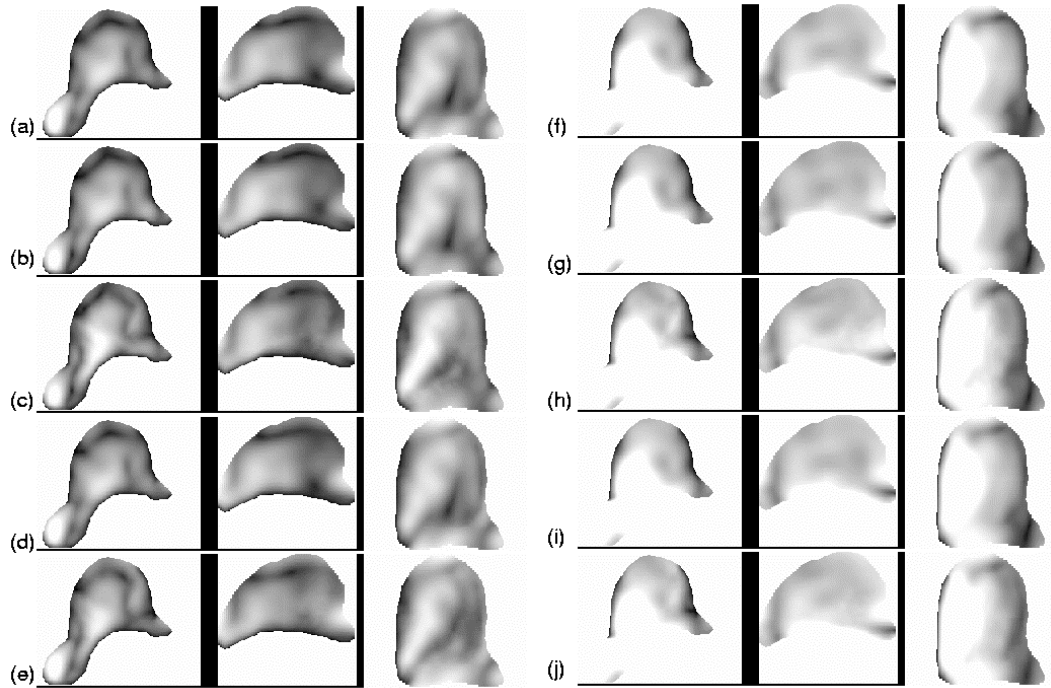
Figure 6 - Orthogonal 2D slices of spatial distribution of displacement error E_T for the FEM models with respect to the 3D non-rigid registration result. Black (white) corresponds to a displacement error of 0mm (5mm). The background is set to white. (a)-(e) BC_2 MM_{1-5}, v=0.495; (f)-(j) BC_3 MM_{1-5}, v=0.495
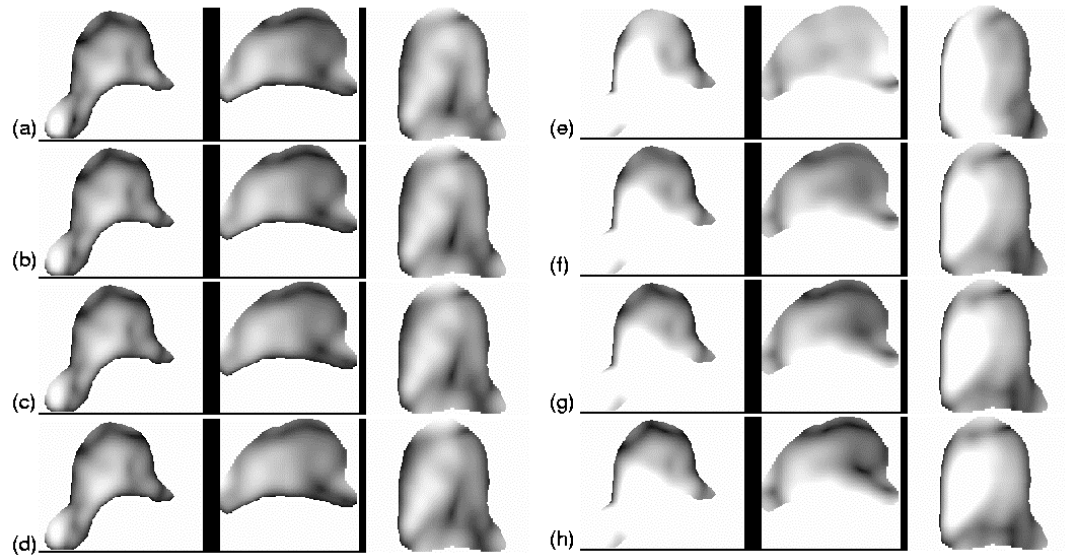
Figure 7 - Orthogonal 2D slices of spatial distribution of displacement error E_T for the FEM models with respect to the non-rigid registration result. Black (white) corresponds to a displacement error of 0mm (5mm). The background is set to white. (a)-(d) BC_2 MM_2, v=0.499, 0.45, 0.4 and 0.3; (e)-(h) BC_3 MM_2, v=0.499, 0.45, 0.4 and 0.3.
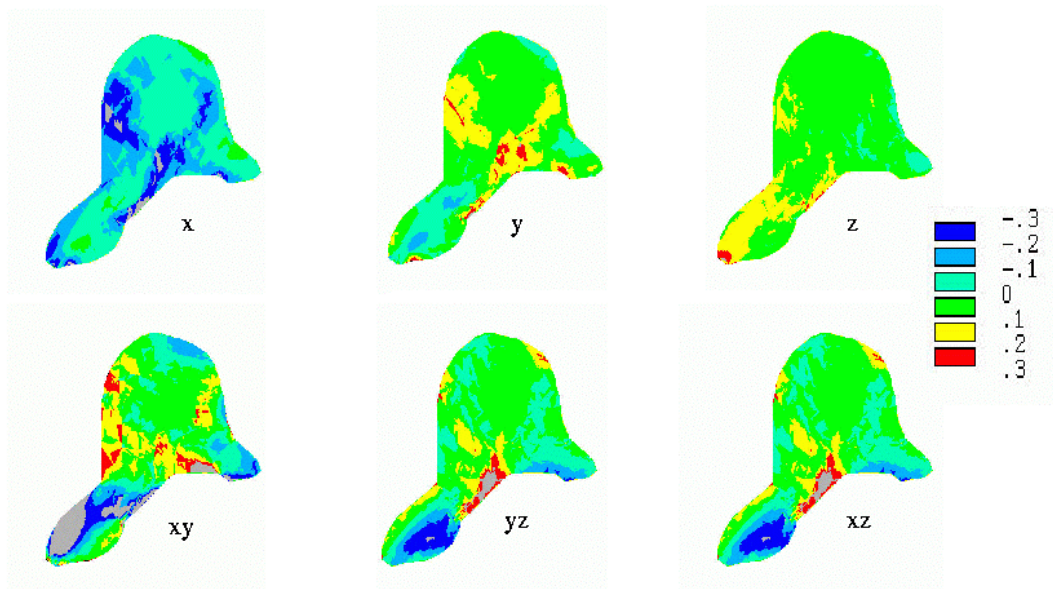

Figure 8 - Axial example slice showing in colour the strain after solving GM_1, MM_3, BC_2, v=0.495 in x, y, z, xy, yz and xz direction. Strains beyond 30% are shown in grey.

E_L, E_V and $E_{|V|}$ (as defined in Section 3.5) were calculated for the quantitative evaluation of the FEM model predictions. The distribution of E_L for each test configuration is shown in Figure 9 by means of boxplots. The initial mean distance error of the landmarks ($\overline{E}_L$) before registration was calculated to be 6.42mm. In comparison, the reproducibility error E_S for the selection of landmarks was 0.31mm and 0.36mm for the image of the uncompressed and compressed breast, respectively. $\overline{E}_L$ reduced to 1.03mm after the 3D non-rigid registration. $\overline{E}_L$ between 1.86mm and 2.67mm can be achieved for correct boundary conditions on medial, lateral and posterior side ($BC_{1,2}$). The maximal error was between 3.19mm and 4.68mm in these cases. Reducing the Poisson's ratio v leads to a reduction of $\overline{E}_L$ from about 4.38mm to 2.93mm for $BC_{3,4}$. This is mainly because a global volume change of about -7% was introduced by $BC_{3,4}$. Additionally, lower Poisson's ratios give the model more flexibility by allowing local volume changes to occur. This facilitated the propagation of the more accurate boundary conditions. Note however, that maximal errors of about 7.5mm are still reported for v=0.3. These errors can be observed close to the posterior side of the breast where inaccurate boundary conditions were applied (see Figure 5 and 7). Higher Poisson's ratios achieved better results for $BC_{5,6,7}$ since no volume change seem to have occurred during the compression. For v=0.499 or v=0.495 an $\overline{E}_L$ between 2.20mm and 2.55mm can be achieved for BC_5 with a maximal error of 5.31mm. Errors increase marginally for BC_6 ($\overline{E}_L$ between 2.25mm and 2.60mm, max(E_L)=5.47mm). As expected, the error increase was more noticeable for BC_7 ($\overline{E}_L$ between 2.40mm and 2.91mm, max(E_L)=6.81mm). None of the material models seem to give an obvious better result with respect to E_L for a given boundary condition and a given Poisson's ratio.
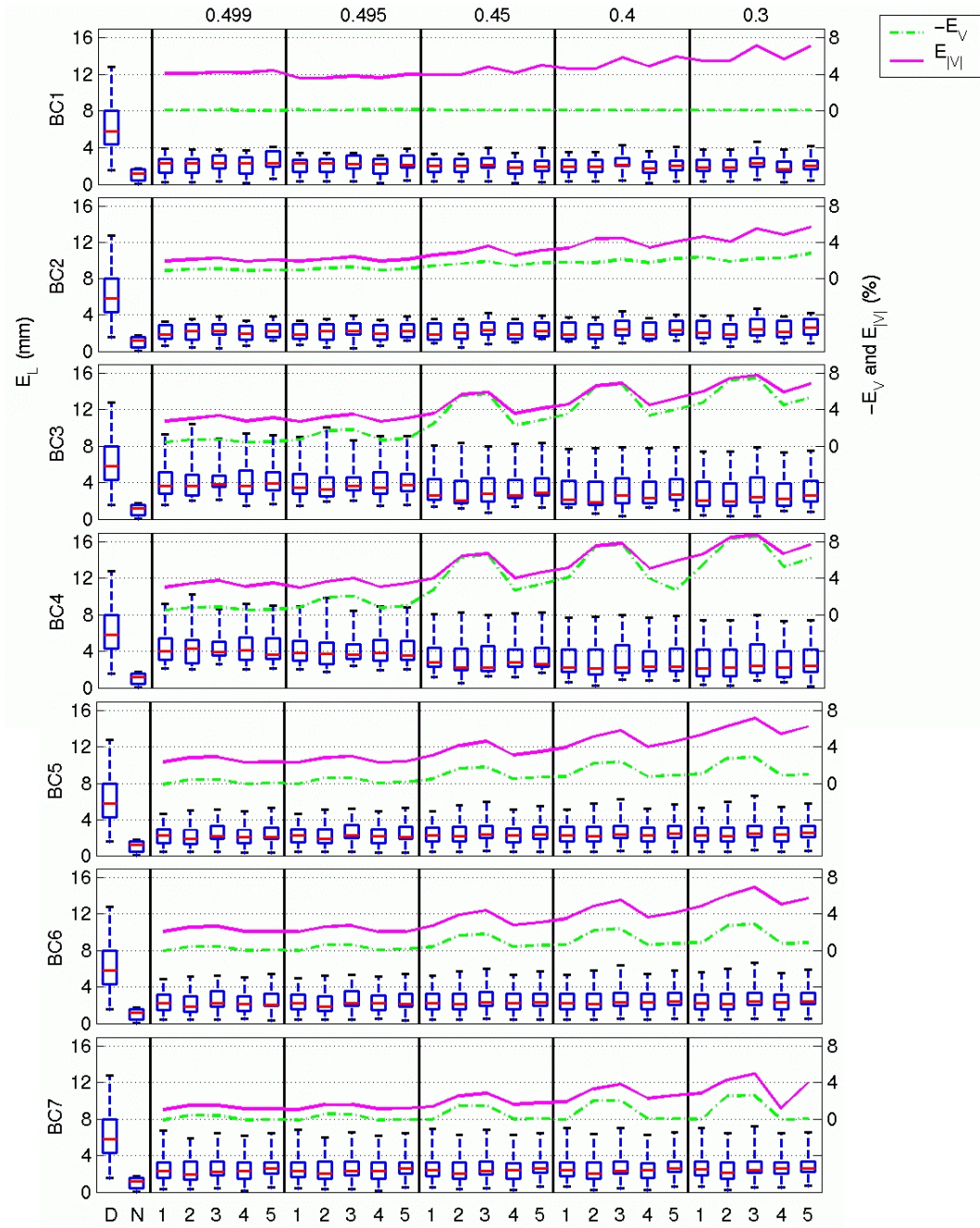
Figure 9 - Results of E_L, $-E_V$ and $E_{|V|}$ for seven boundary conditions (row: BC_1 to BC_7), five Poisson's ratios (main columns: 0.499, 0.495, 0.45, 0.4, 0.3) and five material models (minor columns 1 to 5 in main columns). The first two minor columns show E_L with respect to the original landmark positions (labelled with 'D') and after the 3D non-rigid registration ('N'). The boxplots show the error distribution of E_L in mm of all twelve landmarks. The box has horizontal lines at the lower quartile, median and upper quartile value. The lines extending from each box cover the full range of E_L. The dashed horizontal lines display the negative value of the global volume change ($-E_V$) in %. The solid horizontal lines show the amount of local volume change measured by $E_{|V|}$ in %.

Results for the comparison with respect to different solvers and geometrical models are listed in Table 1. Almost identical results with respect to the landmark error (E_L) are achieved for the different solvers. Note however that the use of the 'Sparse Direct' and the 'Frontal' solver increased the runtime for linear models of GM_1 from approximately 15 minutes to 30 and 140 minutes, respectively, on a 440MHz Sun workstation with 1GByte memory. For non-linear models of GM_1, the increase was from 2.5 hours to 5 and 29 hours, respectively. Table 1 also shows that using a finer mesh did not obviously improve the landmark errors either. The linear and non-linear models of GM_2 were solved with the PCG solver in about 20 and 240 minutes, respectively.

Table 1: Results obtained for BC_2 and v=0.495 with different FEM solvers and with the geometric model GM_2. E_T measures the difference of the transformations obtained by these models to GM_1, BC_2 and v=0.495 solved with the PCG.

	GM_1 PCG solver	GM_1 'Frontal' solver		GM_1 'Sparse Direct' solver		GM_2 PCG solver	
	E_L	E_L	E_T	E_L	E_T	E_L	E_T
	mean (std) max	mean (std) max	mean max	mean (std) max	mean max	mean (std) max	mean max
	mm	mm	mm	mm	mm	mm	mm
MM_1	2.12 (1.01) 3.46	2.12 (1.01) 3.46	0.01 0.11	2.12 (1.01) 3.45	0.01 0.11	2.15 (1.03) 3.46	0.12 3.12
MM_2	2.22 (1.21) 3.77	2.22 (1.21) 3.76	0.00 0.05	2.22 (1.21) 3.77	0.00 0.05	2.23 (1.21) 3.80	0.11 3.11
MM_3	2.49 (1.01) 3.99	2.49 (1.00) 3.99	0.00 0.03	2.49 (1.01) 3.99	0.00 0.03	2.50 (1.02) 4.02	0.16 3.11
MM_4	2.17 (0.98) 3.38	2.17 (0.98) 3.38	0.00 0.00	2.17 (0.98) 3.38	0.00 0.00	2.19 (0.98) 3.32	0.13 3.33
MM_5	2.53 (0.85) 3.86	2.53 (0.85) 3.86	0.00 0.00	2.53 (0.85) 3.86	0.01 0.15	2.53 (0.85) 3.80	0.17 3.27

Conclusion

In this work we have extended the comparison of biomechanical breast models from [23] by assessing the accuracy of predicting the position of internal breast structures when only the displacement on the visible breast surface is known ($BC_{5,6,7}$).

In [22] we had observed that inaccurate assumptions about the surface displacement vectors had a much larger effect on the performance of the FEM breast models than using a model with different tissue properties. This still holds for the range of Poisson's ratios tested in [23].

However, in [23] a major error reduction was noted for inaccurate boundary conditions as the Poisson's ratios were decreased. This was firstly because inaccurate boundary conditions have introduced a volume change. Secondly, the low Poisson's ratios gave the model the local flexibility to propagate the correct boundary conditions. The complete boundary conditions from the non-rigid registration introduced almost no overall volume change (0.07%). Models with accurate boundary conditions on the medial, lateral and posterior side seemed not to be much influenced by the Poisson's ratio apart from the introduction of local and if possible global volume change. We therefore suggest the use of lower Poisson's ratios when the boundary conditions are uncertain or when a volume change is expected. Higher Poisson's ratios seem appropriate for the simulation of breast deformations for validation purposes [18] when volume change should be avoided.

In the work reported here, we observed that it was of advantage to have a good correspondence at the surface of the breast and not to introduce any boundary condition on the posterior side ($BC_{5,6}$) instead of assuming that there was no movement at the posterior side of the breast.

Employing other finite element optimisation strategies did not obviously alter the result. The use of a finer mesh with less badly shaped elements did also not improve the finite element solutions [23].

In further work, we will evaluate different biomechanical breast FEM models on more pre- and post-menopausal volunteers and patients using the same compression protocol. We will also explore the ability of the FEM to predict tissue displacements between a patient lying in prone position with and without compression and the patient lying in supine position without breast fixation. The latter is usually the case in open surgery. We hope that the findings in this work will facilitate the development of further breast registration tools for relating 3D MR images to 2D x-ray projection images, to ultrasound images, and to the patient's position during surgery. Clinically this is important for combining the information provided by images from several modalities or at different times; and for the planning and guidance of interventions.

Acknowledgements

References

[1] ANSYS. http://www.ansys.com.

[2] MAPLE. http://www.maplesoft.com.

[3] Fred S. Azar, Dimitris N. Metaxas, and Mitchell D. Schnall. A Finite Model of the Breast for Predicting Mechanical Deformations during Biopsy Procedure. In *IEEE Workshop on Mathematical Methods in Biomedical Image Analysis, South Carolina, USA*, pages 38–45, 2000.

[4] A. J. Davis. *The Finite Element Method: A First Approach*. Cambridge University Press, Oxford University Press, 1st edition, 1980.

[5] E. R. E. Denton, L. I. Sonoda, D. Rueckert, S. C. Rankin, C. Hayes, M. O. Leach, and D. J. Hawkes. Comparison and Evaluation of Rigid, Affine, and Nonrigid Registration of Breast MR Images. *Journal of Computer Assisted Tomography*, 5:800–805, May 1999.

[6] M. M. Doyley, P. M. Meaney, and J. C. Bamber. Evaluation of an Iterative Reconstruction Method for Quantitative Elastography. *Physics in Medicine and Biology*, 45:1521–1539, 2000.

[7] Matthieu Ferrant, Simon K. Warfield, Charles R. G. Guttmann, Robert V. Mulkern, Ferenc A. Jolesz, and Ron Kikinis. 3D Image Matching Using a Finite Element Based Elastic Deformation Model. In *Medical Image Computing and Computer-Assisted Intervention, Cambridge, UK*, pages 202–209, 1999.

[8] A. Hagemann, K. Rohr, H. S. Stiehl, U. Spetzger, and J. M. Gilsbach. Biomechanical modelling of the human head for physically based, nonrigid registration. *IEEE Transactions on Medical Imaging*, 18(10):875–884, 1999.

[9] Thomas A. Krouskop, Thomas M. Wheeler, Faouzi Kallel, Brian S. Garra, and Timothy Hall. Elastic Moduli of Breast and Prostate Tissues Under Compression. *Ultrasonic Imaging*, 20:260–274, 1998.

[10] A. J. Lawrence, P. J. Rossman, J. L. Mahowald, A. Manduca, L. C. Hartmann, and R. L. Ehman. Assessment of Breast Cancer by Magnetic Resonance Elastography. In *Proceedings of the Seventh Scientific Meeting of the International Society for MR in Medicine, Philadelphia, USA*, page 525, 1999.

[11] Jerrold E. Marsden and Thomas J. R. Huges. *Mathematical Foundations of Elasticity*. Dover Publications, Inc., New York, USA, 1st edition, 1994.

[12] Michael I. Miga, Keith D. Paulsen, Francis E. Kennedy, Alex Hartov, and David W. Roerts. Model-Updated Image-Guided Neurosurgery Using the Finite Element Method: Incorporation of the Falx Cerebri. In *Medical Image Computing and Computer-Assisted Intervention, Cambridge, UK*, pages 900–909, 1999.

[13] Joon Bu Park. *Biomaterials Science and Engineering*. Plenum Press, New York, USA, 1st edition, 1984.

[14] Donald B. Plewes, Jonathan Bishop, Abbas Samani, and Justin Sciarretta. Visualization and Quantization of Breast Cancer Biomechanical Properties with Magnetic Resonance Elastography. *Physics in Medicine and Biology*, 45:1591–1610, 2000.

[15] D. Rueckert, L. I. Sonoda, C. Hayes, D. L. Hill, M. O. Leach, and D. J. Hawkes. Non-rigid Registration using Free-Form Deformations: Application to Breast MR Images. *IEEE Transactions on Medical Imaging*, 7:1–10, August 1999.

[16] Abbas Samani, Jonathan Bishop, Martin J. Yaffe, and Donald B. Plewes. Biomechanical 3D Finite Element Modeling of the Human Breast Using MRI Data. *IEEE Transactions on Medical Imaging*, 20(4):271–279, 2001.

[17] A. Sarvazyan, D. Goukassian, E. Maevsky, and G. Oranskaja. Elastic Imaging as a new Modality of Medical Imaging for Cancer Detection. In *Proceedings of the International Workshop on Interaction of Ultrasound with Biological Media, Valenciennes, France*, pages 69–81, 1994.

[18] J. A. Schnabel, C. Tanner, A. Castellano Smith, M. O. Leach, C. Hayes, A. Degenhard, R. Hose, D. L. G. Hill, and D. J. Hawkes. Validation of Non-Rigid Registration using Finite Element Methods. In *Information Processing in Medical Imaging, Davis, CA, USA*, pages 344–357, 2001.

[19] Will Schroeder, Ken Martin, and Bill Lorensen. *The Visualization Toolkit*. Prentice Hall PTR, New Jersey, USA, 2nd edition, 1998.

[20] R. Sinkus, J. Lorenzen, D. Schrader, M. Lorenzen, M. Dargatz, and D. Holz. High-Resolution Tensor MR Elastography for Breast Tumour Detection. *Physics in Medicine and Biology*, 45:1649–1664, 2000.

[21] Colin Studholme, Derek L. G. Hill, and Dave J. Hawkes. An Overlap Invariant Entropy Measure of 3D Medical Image Alignment. *Pattern Recognition*, 32:71–86, 1999.

[22] C. Tanner, A. Degenhard, J. A. Schnabel, A. Castellano-Smith, C. Hayes, L. I. Sonoda, M. O. Leach, D. R. Hose, D. L. G. Hill, and D. J. Hawkes. A Method for the Comparison of Biomechanical Breast Models. In *IEEE Workshop on Mathematical Methods in Biomedical Image Analysis, Kauai, USA*, pages 11–18, 2001.

[23] C. Tanner, A. Degenhard, J. A. Schnabel, A. Castellano-Smith, C. Hayes, L. I. Sonoda, M. O. Leach, D. R. Hose, D. L. G. Hill, and D. J. Hawkes. A Comparison of Biomechanical Breast Models: A Case Study. In *Proc.SPIE Medical Imaging 2002: Image Processing, San Diego, USA*, to appear, 2002.

[24] P. S. Wellman. *Tactile Imaging*. PhD thesis, Harvard University, 1999.